An enhanced microfluidic control system for improving power density of a hydride-based micro fuel cell

Saeed Moghaddam [a,b,*], Eakkachai Pengwang [a], Richard I. Masel [b], Mark Shannon [a,b]

[a] Mechanical Science and Engineering, 1206 West Green St., University of Illinois, Urbana, IL 61801, United States
[b] Chemical and Biomolecular Engineering, 213 Roger Adams Lab, 600 S. Mathews, Urbana, IL 61801, United States

ABSTRACT

Microfuel cells (MFCs) can potentially power emerging technologies that require power sources in the microliter size range. The recent development of a microfluidic mechanism for self-regulated generation of hydrogen has enabled fabrication of MFCs orders of magnitude smaller than previously possible. In this study, we report an order of magnitude enhancement in the power density of a microliter-scale fuel cell incorporating a new microfluidic design. The microfluidic mechanism is part of an on-board hydrogen generator that uses a reaction between a metal hydride, $LiAlH_4$, and water vapor to generate hydrogen. The hydrogen generated exits the hydride reactor through a porous silicon wall to reach a Nafion-based membrane electrode assembly (MEA). The microfluidic design increased the water vapor release rate to the hydride reactor by one order of magnitude over a previous design. A 9 μL device incorporating the enhanced microfluidic design delivered a power density of $92\,W\,L^{-1}$. Details of a parametric study conducted to improve the water vapor release rate of the microfluidic mechanism and performance analysis of the integrated device are presented in this paper.

Published by Elsevier B.V.

1. Introduction

The need for better energy storage has been widely recognized in applications ranging from micro-devices to large scale systems [1–3]. As better/faster devices and new technologies are being introduced, limitations of the existing power sources are being recognized [4]. Although in some applications increasing functionality has been met by improvements in battery technology or reasonable reduction in time between charges, there are emerging applications (e.g. intelligent insect-sized robots and smart dust) [5–10] that demand far more powerful and smaller (microliter-scale) energy sources than those that exist today. Microfuel cell (MFC) technology that has been under development for some time [11–16] has the potential to bridge this power gap. The energy density of fuels used in MFCs exceeds that of batteries by an order of magnitude (Fig. 1). However, efforts to harvest this high energy density have been hampered by many issues. At the heart of these issues is the architectural complexity of the MFC's that has lead to fabrication, operation, reliability, size, and cost issues.

Recently, we introduced a new fuel cell architecture that allows fabrication of MFCs in the microliter size range. The enabling technology has been a self-regulating microhydrogen generator [17] that delivers hydrogen to a membrane electrode assembly (MEA). The hydrogen generator uses a reaction between a metal hydride (e.g. $LiAlH_4$) and water vapor to generate hydrogen in a reactor. A passive microfluidic control mechanism regulates hydrogen generation through controlled delivery of water vapor to the metal hydride based on the reactor pressure. This self-regulating hydrogen generation and delivery system has eliminated the need for auxiliary components such as pumps, valves, sensors, distribution components, and power and control electronics that made fabrication of microliter-scale fuel cells challenging. We have recently reported [18] fabrication of a fully integrated 9 μL MFC that incorporates the hydrogen generation and control mechanism. The device delivered an energy density of approximately $250\,Wh\,L^{-1}$ and a power density of close to $10\,W\,L^{-1}$. We are currently trying to identify and overcome performance limitations of the device in order to reach our goal of $1000\,Wh\,L^{-1}$ energy density and greater than $500\,W\,L^{-1}$ power density.

In our efforts to improve power density, we have identified, as will be discussed later in this paper, a low hydrogen generation rate due to limited water vapor release by the microfluidic mechanism as a cause of low power density ($\sim 10\,W\,L^{-1}$) in the 1st generation device. In this manuscript, we discuss a design improvement of the microfluidic mechanism that increased the power density of the 2nd generation device by an order of magnitude ($\sim 100\,W\,L^{-1}$) over that of the 1st generation device.

* Corresponding author. Tel.: +1 217 244 5136; fax: +1 217 244 6534.
E-mail addresses: saeedmog@uiuc.edu (S. Moghaddam), epengwa2@uiuc.edu
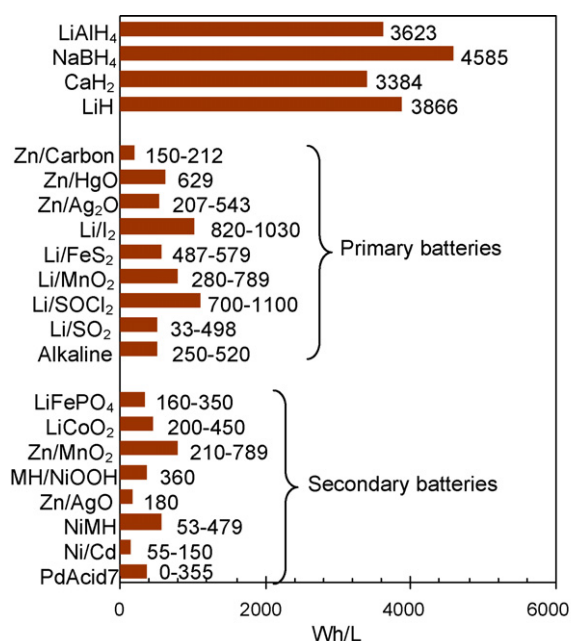(E. Pengwang), r-masel@uiuc.edu (R.I. Masel), mshannon@uiuc.edu (M. Shannon).

Fig. 1. Comparison of the energy density of metal hydrides (operation voltage of 0.7 V is assumed in calculations) and different batteries.

Fig. 3. Cross-sectional view of the hydride reactor porous bottom wall. The image shows only a small section of the 35 μm thick wall.

2. Device architecture

A 3D schematic cross-section of the device is shown in Fig. 2. The device consists of three layers including; (1) water reservoir and vapor release mechanism, (2) hydride reactor, and 3) MEA. Details on the operation principle of the water vapor release mechanism is available in Moghaddam et al. [17]. Briefly, during the device operation, water enters the narrow space between the bottom wall of the reservoir and a membrane through an opening. Capillary forces within the membrane holes keep the water from flowing into the hydride reactor. Water vapor then diffuses into the hydride reactor as shown in the schematic inset in Fig. 2. Hydrogen is generated when water vapor reacts with the hydride. The generated hydrogen then leaves the hydride reactor through a porous silicon wall (with ~5 nm pore size) at the bottom of the reactor and reaches the MEA. If hydrogen is not used by the MEA (i.e. open-circuit
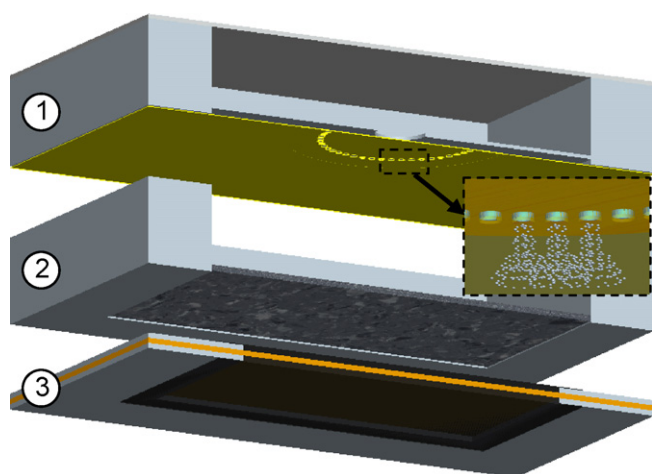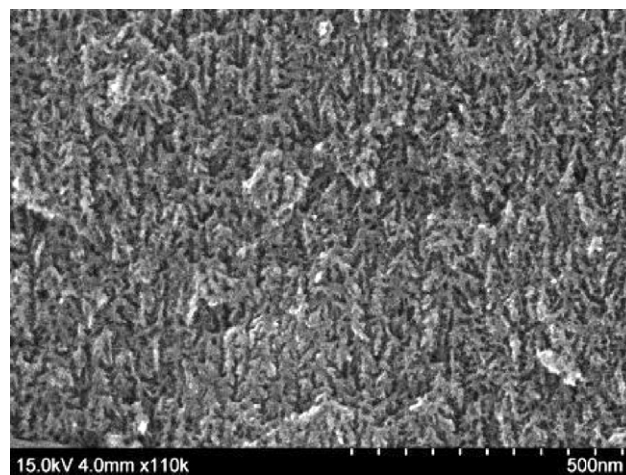
mode), pressure builds up inside the hydride reactor. The membrane is designed to deflect at a pressure less than the capillary forces within the membrane holes. The deflection of the membrane plugs the water port and stops the flow of water from the reservoir. Essentially, the microfluidic control mechanism is a passive valve that automatically regulates hydrogen production based on the hydrogen gas pressure within the hydride reactor.

3. Device fabrication

3.1. Water reservoir and membrane assembly

The water reservoir was fabricated from $\langle 1\,0\,0 \rangle$ silicon using a deep reactive ion etching (DIRE) process. The membrane separating the water reservoir and the hydride reactor was made of polyimide (PI) through spinning and curing PI 5878G (HD Microsystems, Parlin, NJ) on a glass substrate. The final thickness of the PI membrane was 5 μm. Since PI is water permeable, the membrane was sputter-coated with a 0.2 μm thick Cr/Au layer to prevent water diffusion through the membrane when the valve is closed. The circularly distributed array of holes shown in Fig. 2 was etched through the Cr/Au (wet etched) and PI (reactive ion etched) layers. The membrane was transfer-bonded [19] from glass substrate to the bottom of the water reservoir.

3.2. Hydride reactor

The hydride reactor was fabricated from $\langle 1\,0\,0 \rangle$ p-doped silicon using DRIE process. A 20 μm recess was etched at the bottom of the hydride reservoir facing the MEA to facilitate its assembly on the MEA. The bottom wall of the hydride reactor was then anodized in a 25% HF electrolyte to produce ~5 nm diameter pores (Fig. 3) that allow hydrogen to exit the reactor. Typically, 60–70% of the hydride reactor is charged with LiAlH$_4$ (Sigma–Aldrich, Inc., St. Louis, MO). LiAlH$_4$ has the highest reaction rate with water vapor among typical chemical hydrides (e.g. CaH$_2$, NaAlH$_4$, LiBH$_4$, and NaBH$_4$) [20].

3.3. Membrane electrode assembly (MEA)

The MEA was fabricated by sandwiching Nafion® NRE-211 with a nominal thickness of 25 μm (DuPont, Wilmington, DE) between two 25 μm thick stainless steel (SS) foils. The foils had 2 mm × 2 mm square openings to expose Nafion®. The exposed Nafion® membrane was then brush-painted with catalyst. The catalyst ink was prepared by dispersing platinum black HiSPEC 1000 (Alfa Aesar
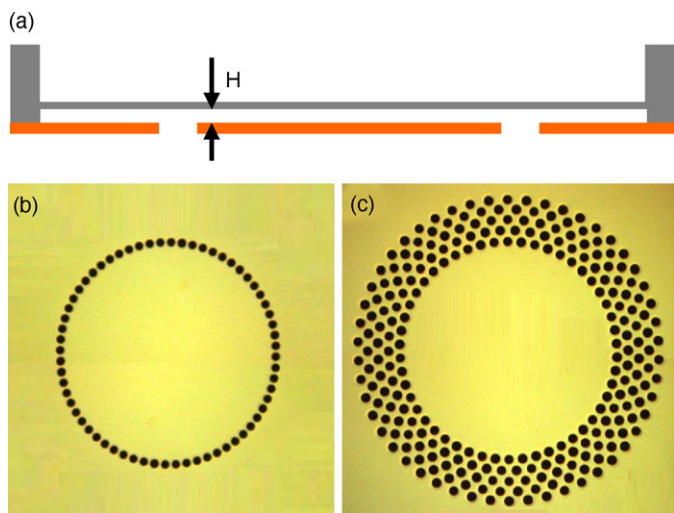
Fig. 2. Cross-section schematic of the device showing its three main components: (1) water reservoir and valve with a stainless steel (SS) cap, (2) hydride reservoir, and (3) membrane electrode assembly (MEA). The inset schematic shows vapor release from the membrane holes. The overall device size is 3 mm × 3 mm × 1 mm, with a total volume of 9 μL.

Fig. 4. Schematic cross-section of the valve (a) and front view of the Cr/Au coated PI membrane showing one row (b) and five rows (c) of 30 μm diameter holes.

Co., Ward Hill, MA) in Nafion® solution, Millipore water, and iso-propanol via sonication. In addition to the membrane area, a small amount of catalyst ink was also painted on the edges of the SS foils around the membrane to provide electrical connection to the SS foils that are also used as current collectors.

3.4. Device assembly

The assembly process of the device was conducted in a glove box. First, the hydride reactor was epoxied (Scotch-Weld 2216 B/A Gray epoxy made by 3M Co., St. Paul, MN) to the MEA. The hydride reactor was then partially filled with LiAlH$_4$. Finally, the water reservoir and membrane assembly were assembled on the hydride chamber. The water reservoir was charged with water outside the glove box.

4. Parametric study of the valve performance

Performance of the valve is determined by a set of parameters including: (1) gap (H) between membrane (when it is not deformed) and bottom of the water reservoir (Fig. 4a), (2) membrane open area, A (Fig. 4b and c), and (3) membrane mechanical properties. Eight test samples were fabricated to study the effect of H and A on the valve water vapor release rate ($\dot{m}$).

The experimental setup shown in Fig. 5 was used to conduct the tests. The setup consists of two main chambers C-1 and C-2. Pressure inside each chamber is adjusted by changing the liquid (Fomblin oil) level in manometers M-1 and M-2. Two push-button valves V-1 and V-2 allow purging the C-2 chamber with dry nitrogen. A humidity sensor (Model SHT75, size 3.7 mm × 2.2 mm × 4.9 mm, supplied by Newark, Chicago, IL) installed on the bottom of the C-2 chamber measures the relative humidity. A typical test involves installing the test sample between the C-1 and C-2 chambers, as depicted in Fig. 5. Water is then supplied to the water reservoir (i.e. topside of the valve). The two chambers were kept at the same pressure. The C-2 chamber is purged with nitrogen until a humidity level of less than 1% is reached. Immediately after purging the chamber (i.e. closing the V-1 and V-2 valves), the chamber humidity starts to rise as the valve releases water vapor.

Variation of $\dot{m}$, calculated using the measured rise in humidity, is shown in Figs. 6 and 7. Results on valves with constant A (one row of 30 μm diameter holes) and different H (3, 13, 26, and 40 μm) suggest (Fig. 6) that increasing H greatly enhances $\dot{m}$ at small H. However, the rate of increase declines at higher H values. In the
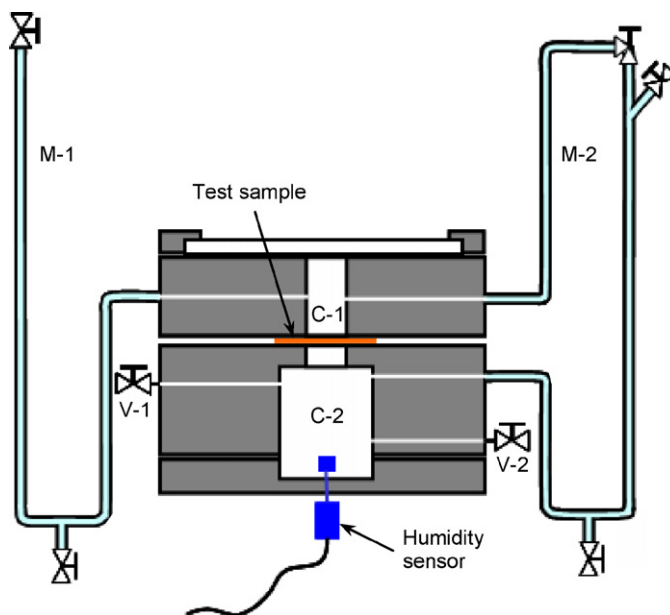

Fig. 5. Schematic of the test setup for measuring the valve performance. Schematic shows the water chamber and membrane assembly held between the top (C-1) and bottom (C-2) chambers of the setup. Two valves (V-1 and V-2) on the C-2 chamber are used for purging it with dry nitrogen. Two manometers (M-1 and M-2) are used to measure and adjust the pressure in C-1 and C-2 chambers.

second set of tests (Fig. 7), samples with different A (four samples with one row of D = 20, 30, 40, and 50 μm holes and a fifth sample with five rows of D = 30 μm holes) and constant H (40 μm) were studied. Overall, increasing A enhanced $\dot{m}$. However, the rate of increase when D was constant deviated from a linear trend seen when D was increased from 20 to 50 μm. We believe that this is due to the fact that increasing D reduces the pressure difference ($\Delta p = 2\sigma \cos\gamma/r$) between the two sides of the membrane resulting in an increase in the actual gap between the membrane and the bottom wall of the reservoir. Note that the actual gap between the membrane and the bottom of the water reservoir is not H.

5. Hydrogen generation rate

To measure the hydrogen generation rate of the hydrogen generator (i.e. water reservoir/valve assembly and hydride chamber
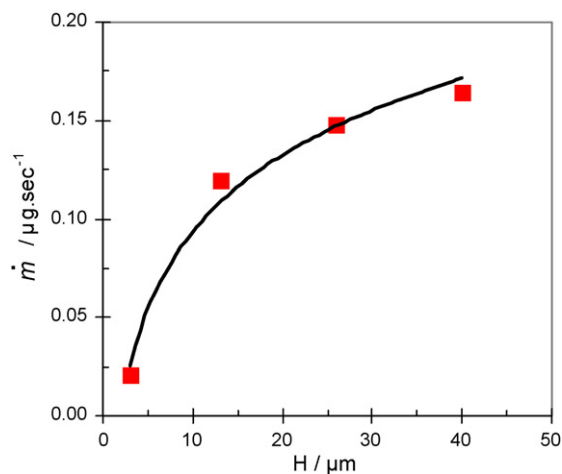

Fig. 6. Water vapor release rate ($\dot{m}$) of four valves with similar membrane open area (A), one row of D = 30 μm holes, and different spacing between membrane and bottom wall of the water reservoir when the membrane in not deformed (H).
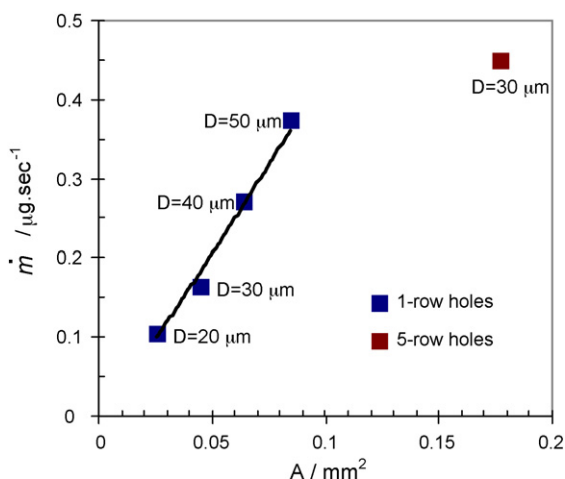
Fig. 7. Water vapor release rate ($\dot{m}$) of different valves as a function of membrane open area (A) and pore size (D) and $H = 40\,\mu m$.

Fig. 9. Hydrogen delivery rate of four hydrogen generators with valves having five rows of $D = 30\,\mu m$ holes and $H = 40\,\mu m$.

shown as components 1 and 2 in Fig. 2) an experimental setup was fabricated (Fig. 8). The setup consists of a main SS fixture for holding the hydrogen generator. An opening on top of the fixture, as shown in Fig. 8a, allows adding water to the water reservoir of the hydrogen generator. The hydrogen exiting the generator (through the porous wall of the hydride reactor) enters a small chamber at the bottom half of the SS fixture that is connected to a plastic U-tube filled with Fomblin liquid. The hydrogen generation rate is calculated by measuring the time it takes for the liquid column to rise from point "A" to "B" (in the right leg of the U-tube shown in Fig. 8c).

To facilitate installation of the hydrogen generator within the main SS fixture, the two components constituting the hydrogen generator were used in their pre-diced form (both part of 8 mm × 8 mm dies that are later diced to 3 mm × 3 mm when integrated into the final fuel cell, shown in Fig. 2). The assembly process was conducted in a glove box. First, hydride reactor was partially filled with LiAlH$_4$. Then the water/valve assembly was epoxied (Scotch-Weld 2216 B/A Gray epoxy made by 3M Co., St. Paul,
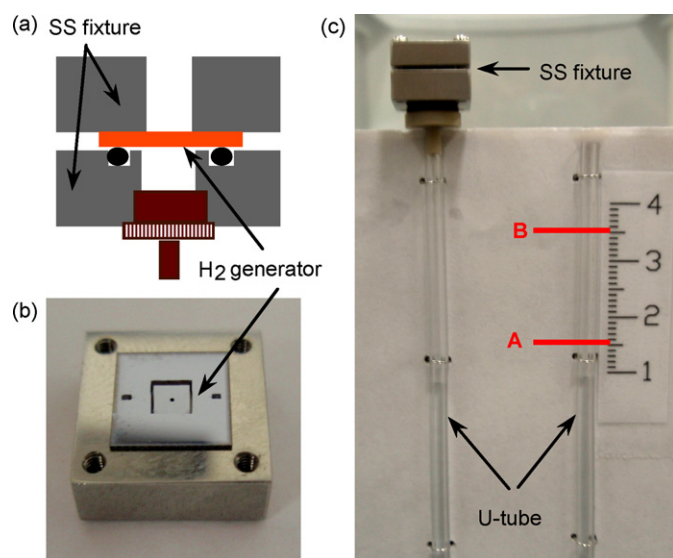

Fig. 8. Experimental setup for measurement of hydrogen generation rate. (a) Schematic of a stainless steel (SS) fixture holding the hydrogen generator, (b) picture of the hydrogen generator sitting on the bottom part of the SS fixture, and (c) picture of the setup. After the liquid level passes marked level "B", the SS fixture is simply detached from the U-tube to avoid Fomblin liquid exiting the U-tube.
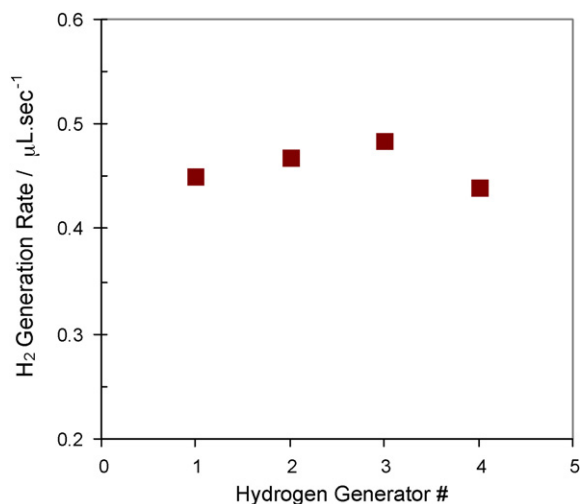
MN) on the hydride chamber. Tests were conducted on hydrogen generators having valves with five rows of $D = 30\,\mu m$ holes and $H = 40\,\mu m$, intended for use in the fully integrated device. The measured hydrogen generation rate of the samples ranged between 0.44 and 0.49 $\mu L\,s^{-1}$ (Fig. 9). This was less than the theoretical value 0.56 $\mu L\,s^{-1}$ calculated using the reaction chemistry between LiAlH$_4$ and water, where

$$H_2O + 0.25LiAlH_4 \rightarrow 0.25LiOH + 0.25Al(OH)_3 + H_2, \qquad (1)$$
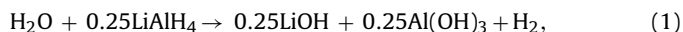
and 0.45 $\mu g\,s^{-1}$ water vapor release rate of the valve. We believe that increased differential pressure across the valve membrane during the test (due to hydrostatic pressure of the rising liquid column in the U-tube) has contributed to lower hydrogen generation rate. In fact, the liquid column rise was limited to less than 25–30 mm to avoid further differential pressure because a 50–60 mm column of Fomblin yields an overall hydrostatic pressure of about 1 kPa.

Since the rate of reaction may be a limiting factor in hydrogen generation, we used Kong et al. [20] data on hydrogen generation rate of LiAlH$_4$ with water vapor for comparison. They measured a hydrogen generation rate of $2.8 \times 10^{-5}\,mol\,g^{-1}\,s^{-1}$ in a 6.5 mm diameter cylindrical reactor made from nickel mesh. In addition, their data showed a constant hydrogen generation rate up to 60% yield after which the rate started to gradually decline, perhaps due to slower water vapor diffusion through the reaction by-products. The thickness of the hydride bed in our reactor is only ~0.3 mm, thus we do not expect a lower hydrogen generation rate than that measured by Kong et al. [20]. Using their results, we determine a hydrogen generation rate of $3.36 \times 10^{-8}\,mol\,s^{-1}$ (our hydride reactor contains approximately 1.2 mg LiAlH$_4$). This is equivalent to 0.76 $\mu L\,s^{-1}$ hydrogen generation rate, which is 65% higher than the average 0.46 $\mu L\,s^{-1}$ that we have observed in our experiment. This information suggests that the reaction rate is less likely to be the limiting factor.

6. Analysis of the integrated device performance

The integrated devices were fabricated (Fig. 10) using valves with five rows of $D = 30\,\mu m$ holes and $H = 40\,\mu m$. Tests were conducted in a chamber (Fig. 11) where humidity was held constant at 60%. Solartron SI 1287 potentiostat was used for operation of the fuel cells. In the first test, a device was operated at a constant voltage of 0.7 V and its output current was measured. As the test results shown in Fig. 12 suggest, the device delivered a relatively steady current with a peak power density of 92 W L^{-1} and an overall energy
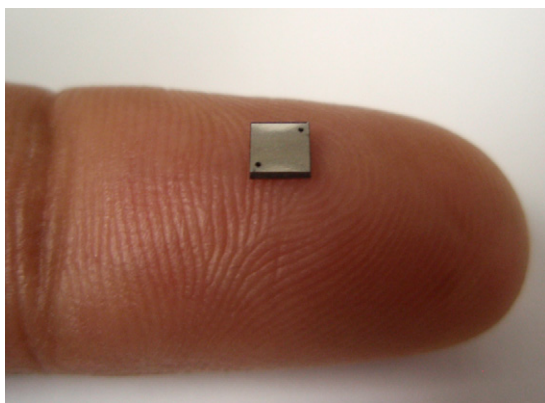
Fig. 10. Picture of a 3 mm × 3 mm × 1 mm fully integrated micro fuel cell (MFC).
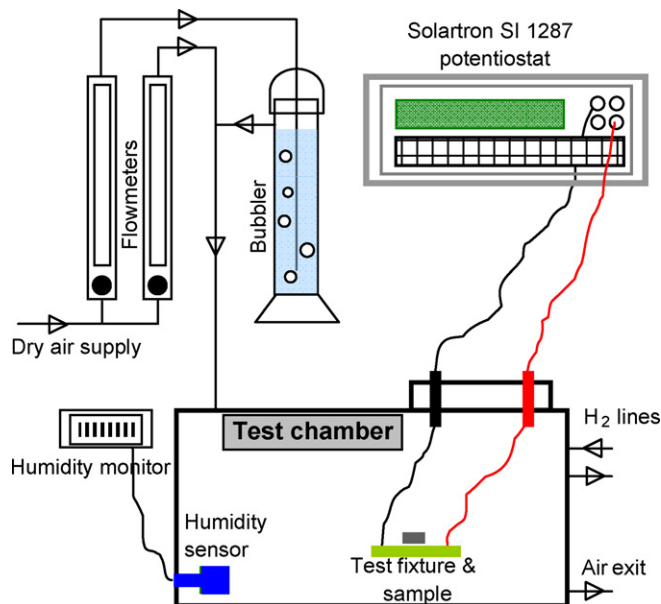

Fig. 11. Experimental apparatus for testing the MEAs and the integrated devices. Humidity of the test chamber was kept constant at 60% in all tests. Hydrogen lines are used during testing the MEA.
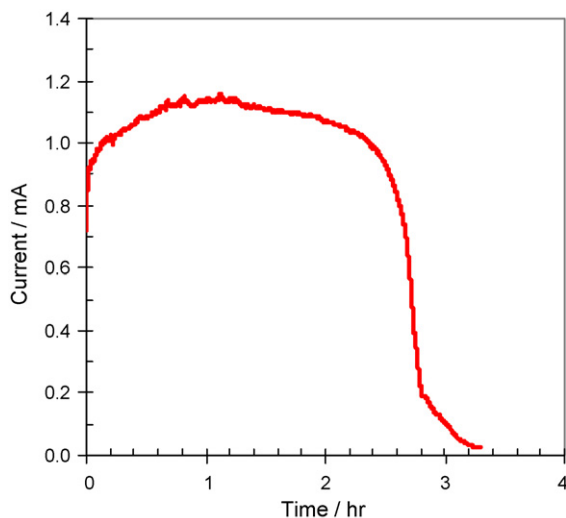

Fig. 12. Current output of an integrated device (operated at 0.7 V) that incorporates a valve with 5 rows of $D = 30\,\mu m$ holes and $H = 40\,\mu m$.
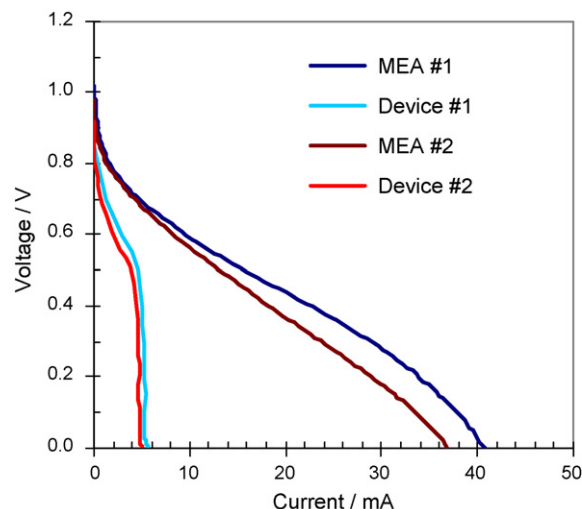

Fig. 13. Comparison of the MEA performance before and after integration into the fully integrated device.

density of 263 Wh L^{-1}. The achieved power density was an order of magnitude higher than the 10 W L^{-1} generated in the 1st generation device [18]. However, the output power was significantly lower than the capability of the MEA as well as the on-board hydrogen generation capacity. The output current of the MEA prior to its integration into the device was 4.5 mA at 0.7 V operating voltage, which is 3.8 times higher than the 1.18 mA generated by the integrated device. The measured current is equivalent to approximately 0.14 μL s^{-1} hydrogen.

As reported in the previous section, the hydrogen generator can deliver a significantly higher rate of hydrogen than the output current of the integrated device suggests. To determine the cause of the integrated device low performance, I–V characteristic performance of the integrated device was determined. Fig. 13 shows the results and their comparison with the I–V performance of the MEAs before integration. The performance curves clearly suggest that the increase in activation (possibly affected by transport limitations) and/or ohmic polarization losses of the MEA is responsible for the lower current output of the integrated device at high operating voltages (above approximately 0.5 V). However, at lower voltages, the device performance becomes limited by the hydrogen generation rate, as evidenced by the almost constant current output of the device. This limiting current density is approximately 5.2 mA, which corresponds to 0.6 μL s^{-1} H$_2$ generation, slightly higher than what was expected on the basis of a water release rate of 0.45 μg s^{-1}. Overall, the results quite convincingly suggest that the water release rate is limiting the device performance.

Based on these results, we have focused our research on finding the causes of MEA deficiency in the integrated device to hopefully increase the device power output by another order of magnitude.

7. Conclusions

This study was conduced to improve power density of a microliter-scale fuel cell. The study was focused on enhancing the hydrogen generation rate inside the device through an increase in the water vapor release rate from a passive microfluidic valve responsible for controlled delivery of water vapor to a hydride reactor (LiAlH$_4$). Effects of geometry on the valve performance were systematically studied. An improved valve design with enhanced water vapor release rate was fabricated and incorporated into a 9 μL device. The device delivered a power density of 92 W L^{-1} (with an overall energy density of 263 Wh L^{-1}), an order of magnitude higher

than the $10\,W\,L^{-1}$ reported in a previous study. Further analysis of the device performance suggested that another factor limiting the power output of the device is significant degradation of the MEA performance after its integration into the fuel cell. Further studies are required to determine the causes of MEA degradation and potential means of overcoming its limitations.

Acknowledgements

References

[1] J.N. Baker, A. Collinson, Power Eng. J. 13 (1999) 107–112.
[2] R.M. Dell, D.A.J. Rand, J. Power Sources 100 (2001) 2–17.
[3] A.S. Arico, P. Bruce, B. Scrosati, J.-M. Tarascon, W. Van Schalkwijk, Nat. Mater. 4 (2005) 366–377.
[4] M. Armand, J.M. Tarascon, Nature 451 (2008) 652–657.
[5] R.J. Wood, IEEE International Conference on Intelligent Robots and Systems, San Diego, CA, United states, 2007, pp. 1889–1894.
[6] S. Bergbreiter, K.S.J. Pister, IEEE International Conference on Robotics and Automation, Piscataway, NJ, USA, 2007, pp. 447–453.
[7] R.R. Selmic, A. Mitra, SPIE—The International Society for Optical Engineering, USA, 2008, pp. 696106-1–696106-13.
[8] S. Hollar, A. Flynn, C. Bellew, K.S.J. Pister, IEEE Micro Electro Mechanical Systems (MEMS), Kyoto, Japan, 2003, pp. 706–711.
[9] A. Boletis, W. Driesen, J.M. Breguet, A. Brunete, IEEE/RSJ International Conference on Intelligent Robots and Systems, Piscataway, NJ, USA, 2006, pp. 5528–5533.
[10] P. Frost Gorder, Computing in Science & Engineering 5 (2003) 6–9.
[11] W. Smith, J. Power Sources 86 (2000) 74–83.
[12] B.C.H. Steele, A. Heinzel, Nature 414 (2001) 345–352.
[13] A. Heinzel, C. Hebling, M. Müller, M. Zedda, C. Müller, J. Power Sources 105 (2002) 250–255.
[14] O.G.J. La, I. Hyun Jin, E. Crumlin, G. Barbastathis, S.-H. Yang, Int. J. Energy Res. 31 (2007) 548–575.
[15] J.D. Morse, Int. J. Energy Res. 31 (2007) 576–602.
[16] A. Kundu, J.H. Jang, J.H. Gil, C.R. Jung, H.R. Lee, S.H. Kim, B. Ku, Y.S. Oh, J. Power Sources 170 (2007) 67–78.
[17] S. Moghaddam, E. Pengwang, R.I. Masel, M.A. Shannon, J. Power Sources 185 (2008) 445–450.
[18] S. Moghaddam, E. Pengwang, K.Y. Lin, R.I. Masel, M.A. Shannon, J. MEMS 17 (2008) 1388–1395.
[19] B.R. Flachsbart, K. Wong, J.M. Iannacone, E.N. Abante, R.L. Vlach, P.A. Rauchfuss, P.W. Bohn, J.V. Sweedler, M.A. Shannon, Lab Chip 6 (2006) 667–674.
[20] V.C.Y. Kong, F.R. Foulkes, D.W. Kirk, J.T. Hinatsu, J. Hydrogen Energy 24 (1999) 665–675.